Baryogenesis induced by magnetic fields during the electroweak phase transition

Yuefeng Di,[1,2] Ligong Bian,[3,*] and Rong-Gen Cai[4,†]

[1]*Institute of Theoretical Physics, Chinese Academy of Sciences, Beijing 100190, China*
[2]*School of Physical Sciences, University of Chinese Academy of Sciences (UCAS), Beijing 100049, China*
[3]*Department of Physics and Chongqing Key Laboratory for Strongly Coupled Physics, Chongqing University, Chongqing 401331, China*
[4]*Institute of Fundamental Physics and Quantum Technology, Ningbo University, Ningbo, 315211, China*

(Received 24 February 2025; revised 26 August 2025; accepted 26 October 2026; published 13 November 2026)

We numerically investigate the first-order electroweak phase transition in the background of a hypermagnetic field with a three-dimensional lattice simulation. The generation of baryon asymmetry is observed, and we present the relationship between baryon number asymmetry and magnetic field strength and its helicity. We find that the magnetic field strength required to achieve the correct matter-antimatter asymmetry is about 10^{-17}–10^{-14} Gauss at present, depending on the correlation length of the helical magnetic field. This study provides a mechanism for explaining the baryon number asymmetry with cosmic magnetic fields.

DOI: 10.1103/lsct-kgkm

I. INTRODUCTION

The matter-antimatter asymmetry remains one of the most fundamental and unresolved puzzles in modern physics. Within the standard cosmological framework, matter and antimatter are postulated to have been created in exact equal abundance during the big bang. However, a subsequent physical process must have disrupted this equilibrium at an early epoch, resulting in the matter-dominated observable Universe. To address this discrepancy, physicists have proposed various baryogenesis scenarios, including electroweak baryogenesis [1,2], leptogenesis [3–5], and the Affleck-Dine mechanism [6,7]. In this work, we propose an alternative baryogenesis paradigm rooted in a first-order phase transition (PT) occurring in a primordial cosmic magnetic field (MF) background. Specifically, the Chern-Simons number N_{CS} initially stored in gauge field configurations is converted into baryon number via the chiral anomaly [8–11], dynamically giving rise to the net cosmic matter-antimatter asymmetry [12–14].

MFs permeate the Universe across diverse scales, from the solar system and the Milky Way [15] to galaxies, galaxy clusters [16–18], and even the cosmic voids of large-scale structure [19–22]. These MFs are hypothesized to originate from primordial seeds generated during high-energy processes in the early Universe, such as inflation [23–29], first-order electroweak PTs [30–36], or the first-order QCD PT [37], followed by various amplification mechanisms and magnetohydrodynamic (MHD) evolutions [38–43]. Primordial MFs leave significant imprints on gamma-ray observations of blazars [43–46], axion dark matter predictions [47], big bang nucleosynthesis [48], and the cosmic microwave background (CMB) spectrum [49–54].

Within the framework of the Standard Model (SM), given the measured Higgs mass of 125 GeV, the electroweak PT is well established to be a crossover [55]. However, if a potential barrier is introduced into the Higgs potential via physics beyond the SM, the transition can be altered into a first-order one [56–58]. This modification provides the crucial "departure from thermal equilibrium," one of the fundamental Sakharov conditions [2,59,60] required to explain the observed matter-antimatter asymmetry, and has consequently become a subject of intense recent investigation [61]. Such a first-order PT proceeds and completes through the nucleation, expansion, and coalescence of true vacuum bubbles (where the vacuum expectation value $v \neq 0$) within the surrounding false vacuum ($v = 0$). Remarkably, the violent collisions of these bubbles not only generate primordial seed magnetic fields but also produce a detectable stochastic gravitational wave background (SGWB) [57,62–65] which can be probed by the next-generation space-based

*Contact author: lgbycl@cqu.edu.cn
†Contact author: cairg@itp.ac.cn

Published by the American Physical Society under the terms of the Creative Commons Attribution 4.0 International license. Further distribution of this work must maintain attribution to the author(s) and the published article's title, journal citation, and DOI. Funded by SCOAP³.

gravitational wave observatories, such as the Laser Interferometer Space Antenna (LISA) [66], Taiji [67], and TianQin [68].

Previous works have shown that MFs modify the Higgs vacuum structure and trigger a vortex condensate known as Ambjørn-Olesen condensation [69–74], affect baryon-number-violating sphaleron processes [75,76] and PT dynamics in the SM [77,78], and drive baryon asymmetry generation via the decay of helical primordial magnetic fields around the electroweak crossover [79,80]. In this work, we observe that bubble dynamics during the first-order electroweak PT drives the conversion of helicity variation in primordial MFs into baryon number via the chiral anomaly, thereby naturally accounting for the baryon asymmetry of the Universe (BAU). Using $(3+1)$-dimensional lattice simulations, we establish a quantitative relation between the resulting baryon asymmetry and the MF strength and determine the present-day MF amplitude required to reproduce the observed matter-antimatter asymmetry. To demonstrate the robustness of our results, we consider two representative helical MF scenarios: infinite correlation length and finite correlation length set to the characteristic mean bubble separation of the first-order electroweak PT.

This work adopts the natural units where $\hbar = c = k_{\mathrm{B}} = 1$. Given the rapid completion of the first-order electroweak PT, we neglect the effects of the cosmic expansion, the evolution of background MFs, and the temperature variation during the PT.

II. FRAMEWORK

To investigate the first-order electroweak PT within a preexisting constant MF background via lattice simulations, we adopt the electroweak Lagrangian extended by the background $\mathrm{U}(1)_{\mathrm{Y}}$ field Y^{μ}_{ex}:

$$\mathcal{L} = (D_\mu\Phi)^\dagger(D^\mu\Phi) - \frac{1}{4}W^a_{\mu\nu}W^{a\mu\nu} - \frac{1}{4}Y_{\mu\nu}Y^{\mu\nu} - \frac{1}{2}Y^{\mathrm{ex}}_{\mu\nu}Y^{\mu\nu} - \mathcal{V}(\Phi). \tag{1}$$

Here, Φ denotes the Higgs doublet, while $W^a_{\mu\nu}$ and $Y_{\mu\nu}$ are the $\mathrm{SU}(2)_{\mathrm{L}}$ and $\mathrm{U}(1)_{\mathrm{Y}}$ field strengths, respectively. $Y^{\mathrm{ex}}_{\mu\nu}$ denotes the constant background MF. In addition, the term $Y^{\mathrm{ex}}_{\mu\nu}Y^{\mu\nu}_{\mathrm{ex}}$ is omitted here as it contributes only a constant energy density. The covariant derivative is given by

$$D_\mu = \partial_\mu - \mathrm{i}g\frac{\sigma^a}{2}W^a_\mu - \mathrm{i}g'\frac{1}{2}(Y_\mu + Y^{\mathrm{ex}}_\mu), \tag{2}$$

where σ^a $(a = 1, 2, 3)$ are the Pauli matrices, and the gauge couplings are set to $g = 0.65$ and $g' = 0.53g$. The fields W^a_μ and $Y^\mu = (Y^0, \mathbf{Y})$ represent the $\mathrm{SU}(2)_{\mathrm{L}}$ and $\mathrm{U}(1)_{\mathrm{Y}}$ gauge bosons, respectively. The potential

$$\mathcal{V}(\Phi) = -\mu^2\Phi^\dagger\Phi + A(\Phi^\dagger\Phi)^{3/2} + \lambda(\Phi^\dagger\Phi)^2 \tag{3}$$

features a cubic term that induces a potential barrier, facilitating a first-order electroweak PT as motivated by some new physics beyond the SM [56–58]. Such a model can be probed by future high-energy colliders [81,82]. The parameters μ^2, A, and λ will be specified below. The initial profile of these bubbles is determined by the potential function (3) using FindBounce [83],

$$\Phi(r) = \frac{v}{2}\left[1 - \tanh\left(\frac{r - R_0}{l_{\mathrm{w}}}\right)\right]\hat{\Phi}, \qquad \dot{\Phi}(r) = 0, \tag{4}$$

where v is the vacuum expectation value of Higgs field, $|\hat{\Phi}| = 1$ has a random SU(2) phase, r is the radial distance from the bubble center, R_0 is the bubble radius, and l_{w} represents the bubble wall thickness. After nucleation, the vacuum bubbles expand and collide with one another, driving the PT forward.

Applying the Euler-Lagrange equations to Eq. (1) and using temporal gauge $W_0 = Y_0 = Y^{\mathrm{ex}}_0 = 0$, we obtain the equations of motion for the Higgs and gauge fields:

$$\partial_0^2\Phi = D_iD_i\Phi - \frac{\partial\mathcal{V}}{\partial\Phi^\dagger}, \tag{5}$$

$$\partial_0^2 W^a_i = -\partial_k W^a_{ik} - g\epsilon^{abc}W^b_k W^c_{ik} + g\,\mathrm{Im}[\Phi^\dagger\sigma^a(D_i\Phi)], \tag{6}$$

$$\partial_0^2 Y_i = -\partial_k Y_{ik} + g'\,\mathrm{Im}[\Phi^\dagger(D_i\Phi)]. \tag{7}$$

During bubble collisions, Φ and $D_i\Phi$ undergo rapid and violent variations, thereby sourcing changes in the gauge fields via Eqs. (6) and (7), which is presented in Ref. [31]. The relationship between the electromagnetic field and the original gauge fields is given by [84]: $A_{\mu\nu} = n^a W^a_{\mu\nu}\sin\theta_W + (Y_{\mu\nu} + Y^{\mathrm{ex}}_{\mu\nu})\cos\theta_W - \mathrm{i}\frac{2}{gv^2}[(D_\mu\Phi)^\dagger(D_\nu\Phi) - (D_\nu\Phi)^\dagger(D_\mu\Phi)]\times \sin\theta_W$ with $n^a = -\Phi^\dagger\sigma^a\Phi/v^2$. This constitutes the core mechanism of magnetic field generation in first-order phase transitions. A strong background MF further enhances this PT-induced MF. We present the corresponding findings in Sec. IV.

Moreover, the evolution of the gauge fields directly governs the dynamics of both the hypermagnetic helicity

$$h_Y = \frac{H_Y}{V} = \frac{1}{V}\epsilon^{ijk}\int \mathrm{d}^3\boldsymbol{x}(Y_i + Y_i^{\mathrm{ex}})(Y_{jk} + Y_{jk}^{\mathrm{ex}}) = \frac{1}{V}\int \mathrm{d}^3\boldsymbol{x}(\boldsymbol{Y} + \boldsymbol{Y}^{\mathrm{ex}})\cdot(\boldsymbol{B}_Y + \boldsymbol{B}_Y^{\mathrm{ex}}) \tag{8}$$

and the Chern-Simons number

$$\frac{N_{\mathrm{CS}}(t)}{V} = \frac{1}{V}\frac{1}{32\pi^2}\epsilon^{ijk}\int \mathrm{d}^3\boldsymbol{x}\left[-g'^2(Y_i + Y_i^{\mathrm{ex}})(Y_{jk} + Y_{jk}^{\mathrm{ex}}) + g^2\left(W_i^a W_{jk}^a - \frac{g}{3}\epsilon^{abc}W_i^a W_j^b W_k^c\right)\right], \tag{9}$$

with $V = L^3$ being the lattice volume. Comparing the above two equations reveals that the hypermagnetic helicity (8) is precisely the U(1) component of N_{CS} (9), up to an overall negative factor. We have verified that the $\mathrm{SU}(2)_{\mathrm{L}}$ contribution to N_{CS} is subdominant, with the explicit results presented in Sec. IV; hence, we restrict our subsequent discussion to the $\mathrm{U}(1)_{\mathrm{Y}}$ component. In the absence of a background hypermagnetic field, the variation of N_{CS} is dominated by the $\boldsymbol{Y}\cdot\boldsymbol{B}_Y$ term, causing it to oscillate around zero. In contrast, when a background hypermagnetic field is present, the initial N_{CS} is nonvanishing and directly proportional to the $\boldsymbol{Y}^{\mathrm{ex}}\cdot\boldsymbol{B}_Y^{\mathrm{ex}}$ term. Furthermore, during the phase transition, the variations in Y_i and Y_{ij} induce shifts in the $\boldsymbol{Y}\cdot\boldsymbol{B}_Y^{\mathrm{ex}}$ and $\boldsymbol{Y}^{\mathrm{ex}}\cdot\boldsymbol{B}_Y$ terms [85]. Provided that the external magnetic field is sufficiently strong, the evolution of N_{CS} becomes pronounced, ultimately settling into a distinct stationary plateau compared to its pretransition value. Our numerical simulations directly substantiate this picture.

The chiral anomaly of the electroweak theory establishes a rigorous topological correspondence between the change in the Chern-Simons number and the baryon number violation during a first-order electroweak PT [8–11],

$$\partial_\mu j_{\mathrm{B}}^\mu = \frac{N_{\mathrm{g}}}{16\pi^2}\left[-g'^2 Y_{\mu\nu}\tilde{Y}^{\mu\nu} + g^2 W_{\mu\nu}^a\tilde{W}^{\mu\nu a}\right] = \frac{N_{\mathrm{g}}}{32\pi^2}\epsilon^{\mu\nu\rho\sigma}\partial_\mu\left[-g'^2 Y_\nu Y_{\rho\sigma} + g^2(W_\nu^a W_{\rho\sigma}^a - \frac{g}{3}\epsilon^{abc}W_\nu^a W_\rho^b W_\sigma^c)\right], \tag{10}$$

where $N_{\mathrm{g}} = 3$ is the number of fermion generations and $\tilde{X}^{\mu\nu} = \frac{1}{2}\epsilon^{\mu\nu\rho\sigma}X_{\rho\sigma}$ denotes the Hodge dual of $X_{\rho\sigma}$. Integrating this equation over a finite time interval and performing the volume average yields a relation between the baryon number density and the variation of the Chern-Simons number:

$$\begin{aligned}\Delta n_{\mathrm{B}} &= \lim_{V\to\infty}\frac{1}{V}\int_0^t \mathrm{d}t\int_V \mathrm{d}^3\boldsymbol{x}\,\partial_\mu j_{\mathrm{B}}^\mu \\ &= \frac{N_{\mathrm{g}}}{32\pi^2}\epsilon^{\mu\nu\rho\sigma}\lim_{V\to\infty}\frac{1}{V}\int_0^t \mathrm{d}t\int_V \mathrm{d}^3\boldsymbol{x}\,\partial_\mu\Big[-g'^2 Y_\nu Y_{\rho\sigma} + g^2(W_\nu^a W_{\rho\sigma}^a - \frac{g}{3}\epsilon^{abc}W_\nu^a W_\rho^b W_\sigma^c)\Big] \\ &= \frac{N_{\mathrm{g}}}{32\pi^2}\epsilon^{ijk}\lim_{V\to\infty}\frac{1}{V}\int_0^t \mathrm{d}t\int_V \mathrm{d}^3\mathbf{x}\,\partial_t\Big[-g'^2 Y_i Y_{jk} + g^2(W_i^a W_{jk}^a - \frac{g}{3}\epsilon^{abc}W_i^a W_j^b W_k^c)\Big] \\ &= N_{\mathrm{g}}\frac{N_{\mathrm{CS}}(t) - N_{\mathrm{CS}}(0)}{V} = N_{\mathrm{g}}\frac{\Delta N_{\mathrm{CS}}(t)}{V}.\end{aligned} \tag{11}$$

In our calculations, we invoke Gauss's divergence theorem and assume that the physical quantities vanish at spatial infinity, such that the total divergence yields a vanishing boundary surface integral, i.e., $\lim_{V\to\infty}\int_V \partial_i J^i d^3\boldsymbol{x} = \lim_{V\to\infty}\oint_{\partial V} J^i dS_i = 0$. Consequently, the interplay between the preexisting background helical hypermagnetic field (HMF) and those generated during the electroweak PT provides a mechanism for BAU generation. This is characterized by the baryon-to-photon ratio

$$\eta_{\mathrm{B}}(t) = \frac{n_{\mathrm{B}}(t)}{s} = \frac{45N_{\mathrm{g}}}{2\pi^2 g_{*S}T^3}\frac{\Delta N_{\mathrm{CS}}(t)}{V}, \tag{12}$$

where $g_{*S} = 106.75$ represents the effective number of entropic degrees of freedom before the PT.

We note that Sakharov's conditions require CP breaking during baryogenesis [59], which need not arise from intrinsic CP-violating Lagrangian terms and can instead be provided by a macroscopic parity-odd background [13,86,87]. In the absence of such a background, sphaleron transitions changing the Chern-Simons number in either direction occur equally often, producing no net baryon asymmetry. A helical hypercharge magnetic field breaks this degeneracy, creating unequal transition rates that accumulate a net Chern-Simons number and hence a baryon asymmetry. The required CP asymmetry therefore originates from the helical magnetic background rather than fundamental CP-violating interactions.

In what follows, we quantitatively investigate how the hyperMF induces changes in the Chern-Simons number via bubble dynamics during the first-order electroweak PT on a $(3+1)$-dimensional lattice and establish the connection between the BAU generated during this process and the helical hyperMF, accounting for its subsequent MHD evolution.

III. SIMULATION SETUP

We numerically solve the equations of motion for the Higgs and gauge fields derived from the Lagrangian in (1). Our simulations are performed on a three-dimensional

TABLE I. Parameters setup in the simulations. Δx and Δt denote the lattice spacing and the time step interval, respectively.

v	Δx	Δt	μ^2	A	λ	R_0	l_w	k_{UV}	k_0	p_{bubble}
1	0.2	0.04	0.68	2.59	1.60	$13\Delta x$	$6\Delta x$	$2\Delta k$	1	5×10^{-8}

spatial lattice with periodic boundary conditions following the strategy of Refs. [31,88–90], utilizing initial conditions based on the thermal fluctuations (refer to Appendixes A and B for details). The code was developed based on that of Ref. [31], where the LATfield2 library [91] and Eigen library [92] are employed. At each time step, every lattice site in the false vacuum state ($\Phi = 0$) has a probability $p_{\rm bubble}$ of nucleating a vacuum bubble with the profile of (4).

To investigate the effect of the background hyperMF on the baryon number, we consider various strengths $B_Y^{\rm ex}$, helicities, and correlation lengths $\lambda_B = \int {\rm d}k k^{-1} E_{BY}(k) / \int {\rm d}k E_{BY}(k)$, where the energy density is defined as $\int {\rm d}k E_{BY}(k) = \int {\rm d}^3\boldsymbol{x} \frac{1}{2}[\boldsymbol{B}_Y^{\rm ex}(\boldsymbol{x})]^2/V$. First, we examine a homogeneous MF with an infinite correlation length, realized by $Y^{{\rm ex}\mu} = (0, 0, xB_Y^{\rm ex}, h_{\rm factor} L B_Y^{\rm ex})$. In this configuration, the field strength is quantized as $B_Y^{\rm ex} = (4\pi/g')N_B L^{-2}$ with $N_B \in \mathbb{Z}$ [93]. We adopt representative values of $N_B = 10, 20, 30, 40$ for our simulations; larger values of N_B are excluded as they significantly suppress the electroweak PT and may prevent its completion [94]. To systematically evaluate the impact of magnetic helicity, we employ three benchmark values for the helicity factor $h_{\rm factor} \in \{0, 1, -1\}$, representing nonhelical, maximally positive, and maximally negative helicity configurations, respectively. Second, we consider a background hyperMF with a finite correlation length following the formalism in Ref. [95]:

$$\tilde{B}_{Yi}^{\rm ex}(\boldsymbol{k}) = B_{\rm ini}(\delta_{ij} - \hat{k}_i\hat{k}_j - {\rm i}\sigma_{\rm M}\epsilon_{iji}\hat{k}_l) g_j(\boldsymbol{k}) \mathcal{P}(k), \quad (13)$$

$$\mathcal{P}(k) = \Theta(k_{\rm UV} - k)(k/k_0)^n. \quad (14)$$

Here, $\Theta(k_{\rm UV} - k)$ is the Heaviside step function, $k_{\rm UV}$ is the ultraviolet cutoff of wave number, k_0 is a reference wave number ensuring that k/k_0 is dimensionless, and $\boldsymbol{g}(\boldsymbol{k})$ is the Fourier transform of a Gaussian random vector field that is δ-correlated in three dimensions, i.e., $g_i(\boldsymbol{x})g_j(\boldsymbol{x}') = \delta_{ij}\delta^3(\boldsymbol{x} - \boldsymbol{x}')$. The MF strength scales as $B_Y^{\rm ex}(x) \propto (k_{\rm UV}/k_0)^{n+3}$, where the spectral index $n \in \{0, 1, 2, 3\}$ corresponds to different physical sources of the primordial MF [43]. The helicity is controlled by $\sigma_{\rm M} \in \{0, 1, -1\}$, representing nonhelical, maximally positive, and maximally negative helicities, respectively; the relationship between the helicity factor, and $\sigma_{\rm M}$ is $h_{\rm factor} = 2\sigma_{\rm M}/(1 + \sigma_{\rm M}^2)$. While the correlation length remains nearly invariant with n in our simulations, it is determined by the lattice size N, with $N = 128$ yielding $\lambda_B \sim R_*/4$ and $N = 512$ yielding $\lambda_B \sim R_*$. Here, R_* denotes the mean bubble separation $R_* = (V/N_b)^{1/3}$, with N_b being the total number of bubbles generated via the bubble nucleation probability $p_{\rm bubble}$. Detailed implementations and derivations of these hyperMFs on the lattice are provided in Appendix. C.

To estimate the BAU generated during the first-order electroweak PT in the presence of a helical hyperMF background, we perform multiple simulations for each parameter set and average the results. Specifically, we conducted 20 simulations for the $N = 128$ lattice, while for $N = 512$, we performed four simulations due to computational constraints. The parameters used in our simulations are summarized in Table. I.

IV. NUMERICAL RESULTS

We first examine the MF generated when bubbles collide with each other, as proposed in Ref. [31] and discussed under Eq. (7). As shown in the left panel of Fig. 1, at the onset of bubble coalescence, the MF exhibits a pronounced enhancement at the collision interfaces. Conversely, the right panel illustrates that after the completion of the PT the MF gradually approaches homogeneity. Figure 2 illustrates the evolution of the PT-induced MF in the presence of a homogeneous background MF. The magnitude of the generated MFs is comparable to that of the background MF. This implies that a stronger background HMF yields a correspondingly stronger generated magnetic field.

We now investigate the Chern-Simons number $N_{\rm CS}$ during the PT associated with the evolution of the PT-induced MF. Figure 3 displays the evolution of $\Delta N_{\rm CS}$ (solid lines) alongside its $\mathrm{U}(1)_{\rm Y}$ component (dashed lines),

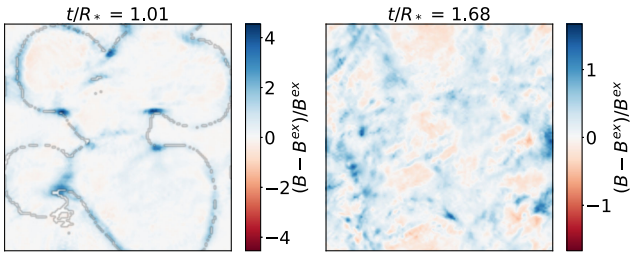


FIG. 1. 2D slice of the background-subtracted MF $(B - B^{\rm ex})/B^{\rm ex}$, corresponding to the specific epoch indicated by the lightest red curve in the top panel of Fig. 2. The early configuration at the onset of bubble coalescence and the late-time snapshot after the completion of the PT are shown in the left and right panels. The white contours denote the position where $|\Phi| = 0.5$, which delineates the locations of the bubble walls.

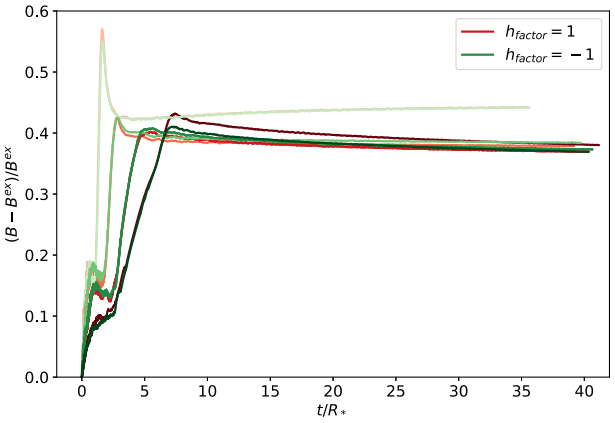


FIG. 2. Evolution of the ratio of the PT-generated MF strength (with the background field subtracted) to the background field strength, $(B - B^{\rm ex})/B^{\rm ex}$, for various homogeneous background MF strengths and helicities.

representing the contribution from the hypermagnetic helicity h_Y. As can be seen, a stronger background MF results in a more pronounced variation in $N_{\rm CS}$. Crucially, the $\mathrm{U}(1)_{\rm Y}$ component provides the dominant contribution to $\Delta N_{\rm CS}$, directly arising from the interaction between the helical background MF and the PT-generated MF, as described by Eqs. (9) and (8). For the background MFs with a finite correlation length, the evolutions of the MF strength and $\Delta N_{\rm CS}$ exhibit similar behavior and are provided in the Appendix. D.

We now investigate the generation of baryon asymmetry during the first-order PT. Figure 4 illustrates the variation of $\eta_{\rm B}$ with respect to the MF strength for a background hyperMF with infinite correlation length. The results in Fig. 4 demonstrate two key findings. First, $\eta_{\rm B}$ increases with the hyperMF strength, indicating enhanced baryon production. Second, the sign of $\eta_{\rm B}$ is determined by the sign of $h_{\rm factor}$; notably, a nonhelical background hyperMF ($h_{\rm factor} = 0$) results in no net baryon production. The data

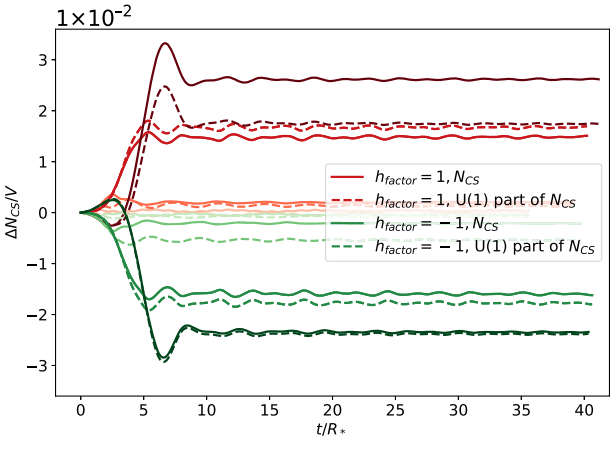


FIG. 3. Time evolution of $\Delta N_{\rm CS}/V$ (solid lines) and its $\mathrm{U}(1)_{\rm Y}$ component (dashed lines). The background MF is homogeneous, with field strength increasing with darker line shades.

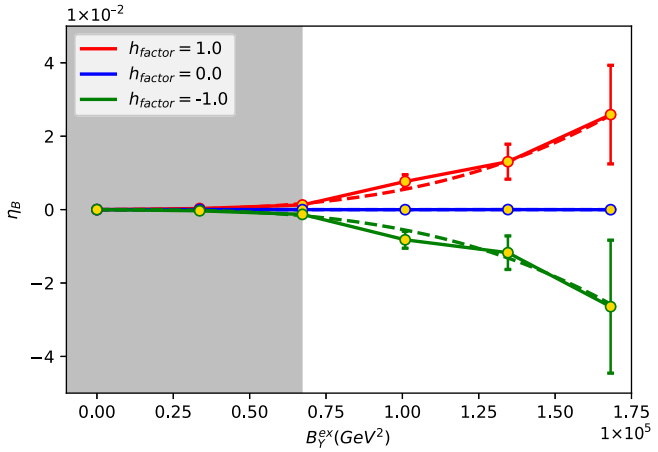


FIG. 4. $\eta_{\rm B}$ as a function of the homogeneous helical hyperMF strength for $h_{\rm factor} = \pm 1, 0$. The dashed line represents the fitting formula Eq. (15). The gray region indicates the MF strengths where Higgs condensation does not occur. Error bars denote the 95% confidence interval of the data.

points in Fig. 4 are fitted by the dashed line, yielding the following relationship:

$$\eta_B = 5.5 \times 10^{-6} h_{\rm factor} \left(\frac{B_Y^{\rm ex}}{10^4\ {\rm GeV}^2} \right)^3. \tag{15}$$

Consequently, to have the observed BAU requires a positive helicity factor $h_{\rm factor}$.

We then consider the scenario of a hyperMF with a finite correlation length comparable to the mean bubble separation. Numerical simulations confirm that as the field energy increases $\eta_{\rm B}$ for $\sigma_{\rm M} = \pm 1$ deviates significantly from zero. In contrast, for the case of $\sigma_{\rm M} = 0$, $\eta_{\rm B}$ vanishes due to the absence of helical effects. The results are presented in Fig. 5, where the dashed lines represent the following fitting relations:

$$\eta_{\rm B} = 2.5 \times 10^{-5} \sigma_{\rm M} \left(\frac{B_{Y,\rm rms}^{\rm ex}}{10^4\ {\rm GeV}^2} \right), \qquad \lambda_B \sim R_*/4. \tag{16}$$

$$\eta_{\rm B} = 3.0 \times 10^{-5} \sigma_{\rm M} \left(\frac{B_{Y,\rm rms}^{\rm ex}}{10^4\ {\rm GeV}^2} \right)^{13/7}, \qquad \lambda_B \sim R_*. \tag{17}$$

Here, $B_{Y,\rm rms}^{\rm ex} = \sqrt{2\rho_{BY}^{\rm ex}}$, where $\rho_{BY}^{\rm ex}$ is the volume-averaged hyperMF energy density. Again, generating the observed BAU requires a positive $\sigma_{\rm M}$.

Inspecting Eqs. (15), (16), and (17), we observe that the prefactors on the right-hand side are consistently of order 10^{-5}, whereas the discrepancies arising from different background hyperMF correlation lengths predominantly manifest in the exponents. Specifically, the exponent equals 3 in the limit of an infinite correlation length but reduces to $13/7$ when the correlation scale is comparable to R_*. Based on this observation, we obtain the BAU as a function of the hyperMF parameters and the phase transition parameter:

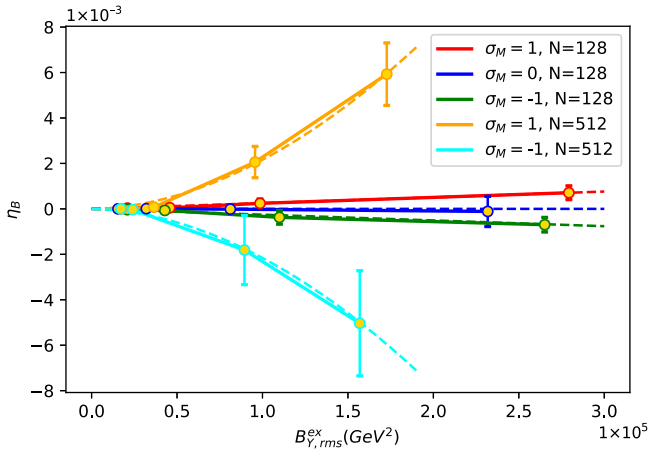


FIG. 5. $\eta_{\rm B}$ as a function of the hyperMF strength for different correlation lengths ($N = 128$ corresponds to $\lambda_B \sim R_*/4$, while $N = 512$ corresponds to $\lambda_B \sim R_*$). The dashed lines represent the fitting formulas of Eqs. (16) and (17), respectively.

$$\eta_{\rm B} \simeq 10^{-5}\sigma_{\rm M}\left(\frac{B^{\rm ex}_{Y,\rm rms}}{10^4\ {\rm GeV}^2}\right)^{\frac{12\lambda_B+R_*}{4\lambda_B+3R_*}}. \tag{18}$$

We observe that the correlation length of the hyperMF significantly influences the power-law dependence of $\eta_{\rm B}$ on $B^{\rm ex}_Y$. Specifically, for hyperMFs with a finite correlation length, a larger mean bubble separation R_* enhances the generation of baryon asymmetry. This process is fundamentally driven by the variation of the Chern-Simons number $N_{\rm CS}$ during the PT, the direction of which is dictated by the sign of $\sigma_{\rm M}$. Further analysis regarding these dynamics and the associated electroweak sphaleron rate is available in the accompanying article [94].

V. COSMOLOGICAL IMPLICATIONS

To facilitate a direct comparison with observational constraints, we have converted the magnetic field strength from GeV^2 to Gauss (1 GeV$^2 \approx 1.95 \times 10^{20}$ Gauss). For a homogeneous MF, independent of its helicity, the MHD evolution follows the scaling law $B_{\rm rec}/B_{\rm EW} = (\tau_{\rm rec}/\tau_{\rm EW})^{-5/7}$ [96], where τ denotes conformal time, and the subscripts "rec" and "EW" correspond to the recombination and electroweak PT epochs, respectively. Following recombination, the MF evolves adiabatically, during which the comoving field strength and correlation length remain constant. By integrating this scaling with Eq. (18), we find that a homogeneous helical MF capable of generating the observed baryon asymmetry corresponds to a present-day field strength of approximately 5.2×10^{-18} Gauss.

For MFs with finite correlation lengths under fully helical conditions, the comoving correlation scale evolves as $\lambda_{\rm rec}/\lambda_{\rm EW} = (\tau_{\rm rec}/\tau_{\rm EW})^{2/3}$, while the comoving MF strength scales as $B_{\rm rec}/B_{\rm EW} = (\tau_{\rm rec}/\tau_{\rm EW})^{-1/3}$ [96–98]. By applying Eq. (18) and evolving the physical quantities

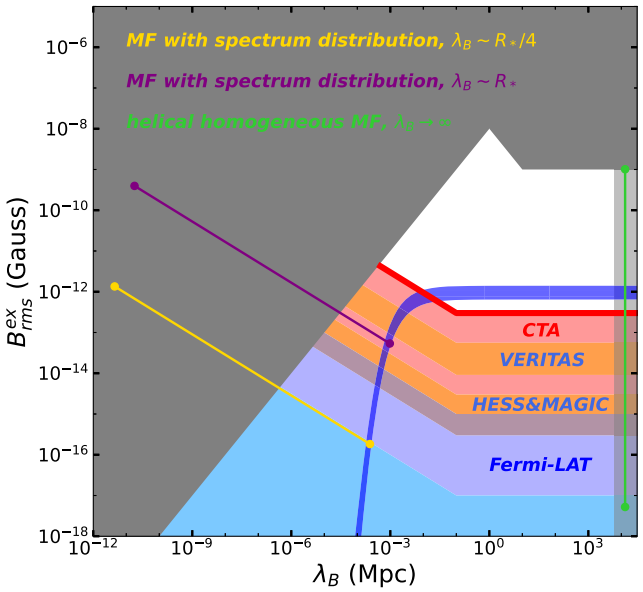


FIG. 6. The yellow, purple, and green lines illustrate the MHD evolution of the MF strength and correlation length required to yield the observed baryon asymmetry. The blue band denotes the parameter space for these values based on Eq. (18). The light gray region on the right indicates the Hubble scale. The gray region is excluded by MHD turbulent decay and CMB anisotropy measurements [43]. The projected sensitivity of the Cherenkov Telescope Array (CTA) to intergalactic MF (IGMF) strength is indicated by the red region [99]. Orange regions are excluded at the 95% to 99% confidence levels by H. E. S. S. [100], MAGIC [101], and VERITAS [102] observations. Dark and light blue regions are excluded by the lower bounds on IGMF strength from Fermi-LAT [45,103]. All physical quantities have been redshifted to their present-day values.

to their present-day values ($B^{\rm ex}_{\rm rms} = g' B^{\rm ex}_{Y,\rm rms}/e$), we determine the parameter space required to produce the observed baryon asymmetry. Specifically, for correlation lengths in the range $\lambda_B \in [2.4 \times 10^{-4}, 9.6 \times 10^{-4}]$ Mpc, the required MF strength is $B^{\rm ex}_{\rm rms} \in [1.8 \times 10^{-16}, 5.3 \times 10^{-14}]$ Gauss. This viable parameter space is represented by the blue band in Fig. 6. Notably, a significant portion of this region remains consistent with current observational constraints. Consequently, a first-order electroweak PT in the presence of a background hyperMF provides a robust and viable mechanism for explaining the origin of the matter-antimatter asymmetry in the Universe.

VI. CONCLUSIONS

In this work, we numerically investigated the first-order electroweak PT in the presence of a background hyperMF. Our results show that a helical hyperMF provides an efficient mechanism for generating baryon asymmetry. We established a quantitative relationship between the resulting asymmetry and the hyperMF properties, demonstrating that to achieve the observed matter-antimatter asymmetry a homogeneous background MF would require

a present-day strength of approximately 4.6×10^{-18} Gauss. For a spectrum-distributed MF, the required field strength lies within the range of 10^{-16} to 10^{-14} Gauss, with a corresponding correlation length of 10^{-4} to 10^{-3} Mpc. Such values are within a range that can be effectively probed by Fermi-LAT gamma-ray observations.

A key distinction of our work from the previous studies, such as Refs. [79,80,104], lies in the underlying mechanism of baryon asymmetry generation. In our scenario, the MF generated during the first-order electroweak PT, acting in concert with the preexisting helical hyperMF, ensures the time variation of the hypermagnetic helicity and the Chern-Simons number. This dynamic evolution serves as the primary driver for baryon asymmetry. In contrast, earlier studies attributed the asymmetry to the decay of MF helicity prior to the Standard Model crossover, a mechanism that necessitates an MF strength of approximately 10^{-17} Gauss at a much smaller correlation length of 10^{-3} pc.

For the case of a homogeneous hyperMF, we further observed that the Higgs field forms a hexagonally arranged vortex lattice when $g' B_Y^{\rm ex}/m_W^2 \gtrsim 3$, independent of whether the MF is helical. This behavior aligns with the Ambjørn-Olesen condensation phenomenon [69–72] predicted within the Standard Model framework. The absence of this effect in Ref. [78] regarding the first-order electroweak PT may be attributed to significant fluctuations in their specific configurations. Recent numerical confirmation of this phenomenon in the SM crossover case is provided in Ref. [74]. In contrast, for hyperMFs with finite correlation lengths, the inherent randomness of the field configuration prevents the formation of a coherent Ambjørn-Olesen condensate. Further details on the PT dynamics and Ambjørn-Olesen condensation in the background of the hyperMF are available in the accompanying article [94]. Although our lattice resolution is sufficient for the bubble wall that is comparable with the width of the electroweak string, we did not observe the formation of them as proposed in Refs. [105–108]. This discrepancy likely arises because our simulations did not impose any prior ansatz on the gauge fields, distinguishing our approach from the methodologies employed in those studies. Physically, this is because that the electroweak string is unstable when the Higgs mass is larger than that of the Z boson [109–111]. Therefore, the link between electroweak strings and baryogenesis established through the relationship between the Chern-Simons number and the MF helicity of the Z field [105–108] is invalid anymore.

We hope that our study provides valuable insights for future observations of cosmic MFs and contributes to uncovering new physics beyond the Standard Model. It is important to note that our current simulations do not account for the effect of the expansion of the Universe and relativistic fluid, both of which could influence the dynamics of the first-order electroweak PT. These factors warrant further investigation. Additionally, the gravitational waves generated by PTs in the presence of background MFs may exhibit distinct signatures compared to those without preexisting magnetic fields, offering another promising avenue for future research.

The simulation strategy developed in this work is readily generalizable to studying the evolution of topological defects—such as cosmic strings and domain walls—within a primordial MF background. These defects are considered as potential cosmic origins of the SGWB recently observed in the NANOGrav datasets [112,113].

The numerical calculations in this study were carried out on the ORISE Supercomputer.

ACKNOWLEDGMENTS

L. B. is supported by the National Natural Science Foundation of China (NSFC) under Grants No. 12322505 and No. 12547101. L. B. also acknowledges Chongqing Natural Science Foundation under Grant No. CSTB2024NSCQ-JQX0022. R. G. C. is supported by the National Natural Science Foundation of China Grants No. 12588101 and No. 12235019.

DATA AVAILABILITY

There are no publicly available research data or software supporting this manuscript. Requests for further information or data should be sent to the authors.

APPENDIX A: EQUATIONS OF MOTION ON LATTICE

Under the temporal gauge $W_0^a = Y_0 = Y_0^{\rm ex} = 0$, the action on the lattice is

$$\begin{aligned} S = \sum_{x,t} \Delta t \Delta x^3 \Bigg\{ & (D_0\Phi)^\dagger (D_0\Phi) - \sum_i (D_i\Phi)^\dagger (D_i\Phi) - \mathcal{V}(\Phi) + \left(\frac{2}{g\Delta t \Delta x}\right)^2 \sum_i \left(1 - \frac{1}{2}{\rm Tr} U_{0i}\right) \\ & + \left(\frac{2}{g'\Delta t \Delta x}\right)^2 \sum_i (1 - {\rm Re} V_{0i}) - \frac{2}{g^2 \Delta x^4} \sum_{i,j} \left(1 - \frac{1}{2}{\rm Tr} U_{ij}\right) - \frac{2}{g'^2 \Delta x^4} \sum_{i,j} (1 - {\rm Re} V_{ij}) \Bigg\} \\ & + \left(\frac{2}{g'\Delta t \Delta x}\right)^2 \sum_i ({\rm Im}\, V_{0i})({\rm Im}\, V_{{\rm ex}0i}) - \frac{2}{g'^2 \Delta x^4} \sum_{i,j} ({\rm Im}\, V_{ij})({\rm Im}\, V_{{\rm ex}ij}). \end{aligned} \tag{A1}$$

The Higgs field Φ is defined on the lattice sites, while the gauge fields are defined on the links between two adjacent sites by link fields:

$$U_i(t,x) = \exp\left[-\mathrm{i}g\Delta x\frac{\sigma^a}{2}W_i^a(t,x)\right], \tag{A2}$$

$$V_i(t,x) = \exp\left[-\mathrm{i}g'\Delta x\frac{1}{2}Y_i(t,x)\right], \tag{A3}$$

$$V_i^{\mathrm{ex}}(t,x) = \exp\left[-\mathrm{i}g'\Delta x\frac{1}{2}Y_i^{\mathrm{ex}}(t,x)\right]. \tag{A4}$$

Higgs field and gauge fields are defined on the exact time step, and their canonical momenta Π, E, and F are defined halfway between the time steps.

We use $x+i$ to denote a space step forward toward the i direction and $x-i$ to denote a space step backward. The link fields, $U_i(t,x), V_i(t,x), V_i^{\mathrm{ex}}(t,x)$, parallel transport the Higgs field Φ that are located at site $x+i$ back to site x, and their Hermitian conjugate parallel transport the Higgs field Φ that are located at site x to site $x+i$. Therefore, using the leapfrog algorithm, the covariant derivative of $\Phi(t,x)$ is

$$\begin{aligned}
D_i\Phi &= \frac{1}{\Delta x}[U_i(t,x)V_i(t,x)V_{\mathrm{ex}i}(t,x)\Phi(t,x+i) - \Phi(t,x)],\\
D_0\Phi &= \frac{1}{\Delta t}[U_0(t,x)V_0(t,x)V_{\mathrm{ex}0}(t,x)\Phi(t+\Delta t,x) - \Phi(t,x)]\\
&= \frac{1}{\Delta t}[\Phi(t+\Delta t,x) - \Phi(t,x)].
\end{aligned}$$

The plaquette fields with all space indices are

$$\begin{aligned}
U_{ij}(t,x) &= U_j(t,x)U_i(t,x+j)U_j^\dagger(t,x+i)U_i^\dagger(t,x),\\
V_{ij}(t,x) &= V_j(t,x)V_i(t,x+j)V_j^\dagger(t,x+i)V_i^\dagger(t,x),\\
V_{\mathrm{ex}ij}(t,x) &= V_{\mathrm{ex}j}(t,x)V_{\mathrm{ex}i}(t,x+j)V_{\mathrm{ex}j}^\dagger(t,x+i)V_{\mathrm{ex}i}^\dagger(t,x).
\end{aligned}$$

The plaquette fields with one time index are

$$\begin{aligned}
U_{0i}(t,x) &= U_i(t,x)U_0(t+\Delta t,x)U_i^\dagger(t+\Delta t,x)U_0^\dagger(t,x) = U_i(t,x)U_i^\dagger(t+\Delta t,x),\\
V_{0i}(t,x) &= V_i(t,x)V_0(t+\Delta t,x)V_i^\dagger(t+\Delta t,x)V_0^\dagger(t,x) = V_i(t,x)V_i^\dagger(t+\Delta t,x),\\
V_{\mathrm{ex}0i}(t,x) &= V_{\mathrm{ex}i}(t,x)V_{\mathrm{ex}0}(t+\Delta t,x)V_{\mathrm{ex}i}^\dagger(t+\Delta t,x)V_{\mathrm{ex}0}^\dagger(t,x) = V_{\mathrm{ex}i}(t,x)V_{\mathrm{ex}i}^\dagger(t+\Delta t,x).
\end{aligned}$$

Setting the functional derivative of action (A1) to zero yields equations of motion:

$$\begin{aligned}
\Pi(t+\Delta t/2,x) = \Pi(t-\Delta t/2,x) + \Delta t\Bigg\{&\frac{1}{\Delta x^2}\sum_i[U_i(t,x)V_i(t,x)V_{\mathrm{ex}i}(t,x)\Phi(t,x+i),\\
&- 2\Phi(t,x) + U_i^\dagger(t,x-i)V_i^\dagger(t,x-i)V_{\mathrm{ex}i}^\dagger(t,x-i)\Phi(t,x-i)] - \frac{\partial\mathcal{V}}{\partial\Phi^\dagger}\Bigg\},
\end{aligned} \tag{A5}$$

$$\begin{aligned}
\mathrm{Im}[E_k(t+\Delta t/2,x)] = \mathrm{Im}[E_k(t-\Delta t/2,x)] + \Delta t\Bigg\{&\frac{g'}{\Delta x}\mathrm{Im}[\Phi^\dagger(t,x+k)U_k^\dagger(t,x)V_k^\dagger(t,x)V_{\mathrm{ex}k}^\dagger(t,x)\Phi(t,x)]\\
&- \frac{2}{g'\Delta x^3}\sum_i \mathrm{Im}[V_k(t,x)V_i(t,x+k)V_k^\dagger(t,x+i)V_i^\dagger(t,x)\\
&+ V_i(t,x-i)V_k(t,x)V_i^\dagger(t,x+k-i)V_k^\dagger(t,x-i)]\Bigg\},
\end{aligned} \tag{A6}$$

$$\mathrm{Tr}[i\sigma^m F_k(t+\Delta t/2,x)] = \mathrm{Tr}[i\sigma^m F_k(t-\Delta t/2,x)] + \Delta t\Big\{\frac{g}{\Delta x}\mathrm{Re}[\Phi^\dagger(t,x+k)U_k^\dagger(t,x)V_k^\dagger(t,x)V_{\mathrm{ex}k}^\dagger(t,x)i\sigma^m\Phi(t,x)]$$
$$-\frac{1}{g\Delta x^3}\sum_i \mathrm{Tr}[i\sigma^m U_k(t,x)U_i(t,x+k)U_k^\dagger(t,x+i)U_i^\dagger(t,x)$$
$$+ i\sigma^m U_k(t,x)U_i^\dagger(t,x+k-i)U_k^\dagger(t,x-i)U_i(t,x-i)]\Big\}. \tag{A7}$$

The conjugate momenta relate to field updates via

$$\Phi(t+\Delta t,x) = \Phi(t,x) + \Delta t\Pi(t+\Delta t/2,x), \tag{A8}$$

$$V_i(t+\Delta t,x) = \frac{1}{2}g'\Delta x\Delta t E_i(t+\Delta t/2,x)V_i(t,x), \tag{A9}$$

$$U_i(t+\Delta t,x) = g\Delta x\Delta t F_i(t+\Delta t/2,x)U_i(t,x). \tag{A10}$$

Note that $V_{\mathrm{ex}i}(t,x)$ is static and thus lacks a conjugate momentum.

Gauss constraints derived similarly are

$$\Delta\mathcal{G}_{\mathrm{U}(1)}(t,x) = \frac{1}{\Delta x}\sum_i \mathrm{Im}[E_i(t,x) - E_i(t,x-i)] - g'\,\mathrm{Im}[\Pi^\dagger(t,x)\Phi(t,x)] = 0, \tag{A11}$$

$$\Delta\mathcal{G}^m_{\mathrm{SU}(2)}(t,x) = \frac{1}{\Delta x}\mathrm{Tr}\sum_i \mathrm{i}\sigma^m[F_i(t,x) - U_i^\dagger(t,x-i)F_i(t,x-i)U_i(t,x-i)] - g\mathrm{Re}[\Pi^\dagger(t,x)\mathrm{i}\sigma^m\Phi(t,x)] = 0. \tag{A12}$$

We employ

$$\Delta\mathcal{G}^2(t) = \sum_x\{[\Delta\mathcal{G}_{\mathrm{U}(1)}(t,x)]^2 + [\Delta\mathcal{G}^1_{\mathrm{SU}(2)}(t,x)]^2 + [\Delta\mathcal{G}^2_{\mathrm{SU}(2)}(t,x)]^2 + [\Delta\mathcal{G}^3_{\mathrm{SU}(2)}(t,x)]^2\} \tag{A13}$$

to quantify the degree of Gauss constraint violation. Throughout the simulation, the variation of $\Delta\mathcal{G}^2(t)$ remains strictly bounded below 10^{-17}.

APPENDIX B: INITIALIZATION

Before the PT occurs, we assume that the Higgs field is in thermal equilibrium. Therefore, we can use the thermal spectrum to describe the amplitude and momentum distribution of each scalar component Φ_i of the Higgs doublet Φ and each scalar component Π_i of the conjugate momentum field Π in momentum space

$$\mathcal{P}_{\Phi_i}(k) = \frac{1}{\omega_k}\frac{1}{e^{\omega_k/T}-1}, \qquad \mathcal{P}_{\Pi_i}(k) = \frac{\omega_k}{e^{\omega_k/T}-1}, \tag{B1}$$

and

$$\Phi = \frac{1}{\sqrt{2}}\begin{pmatrix}\Phi_1+\mathrm{i}\Phi_2\\ \Phi_3+\mathrm{i}\Phi_4\end{pmatrix}, \qquad \Pi = \frac{1}{\sqrt{2}}\begin{pmatrix}\Pi_1+\mathrm{i}\Pi_2\\ \Pi_3+\mathrm{i}\Pi_4\end{pmatrix}, \tag{B2}$$

where $(e^{\omega_k/T}-1)^{-1}$ is the occupation number of the Bose-Einstein distribution, $\omega_k = \sqrt{k^2+m_{\mathrm{eff}}^2}$ is the physical frequency, and k and m_{eff} are physical momentum and effective mass of the Higgs field.

In the continued limit, we have

$$\langle\Phi_i(\boldsymbol{k})\Phi_j(\boldsymbol{k}')\rangle = (2\pi)^3\mathcal{P}_{\Phi_i}(k)\delta(\boldsymbol{k}-\boldsymbol{k}')\delta_{ij}, \tag{B3}$$

$$\langle\Pi_i(\boldsymbol{k})\Pi_j(\boldsymbol{k}')\rangle = (2\pi)^3\mathcal{P}_{\Pi_i}(k)\delta(\boldsymbol{k}-\boldsymbol{k}')\delta_{ij}, \tag{B4}$$

$$\langle\Phi_i(\boldsymbol{k})\Pi_j(\boldsymbol{k}')\rangle = 0. \tag{B5}$$

Converting it into a discrete form on the lattice, we get

$$\langle|\Phi_i(\boldsymbol{k})|^2\rangle = \left(\frac{N}{\Delta x}\right)^3\mathcal{P}_{\Phi_i}(k), \qquad \langle\Phi_i(\boldsymbol{k})\rangle = 0, \tag{B6}$$

$$\langle|\Pi_i(\boldsymbol{k})|^2\rangle = \left(\frac{N}{\Delta x}\right)^3\mathcal{P}_{\Pi_i}(k), \qquad \langle\Pi_i(\boldsymbol{k})\rangle = 0, \tag{B7}$$

where N denotes the number of points per side and Δx is the physical lattice spacing. $\Phi_i(\boldsymbol{k})$ and $\Pi_i(\boldsymbol{k})$ satisfy the Gaussian distribution in the momentum space that varies from point to point and contain all modes from the infrared

truncation $k_{\rm IR} = \Delta k = 2\pi/(N\Delta x)$ to the ultraviolet cutoff $k_{\rm UV}$.

For the gauge fields, we set their initial values to 0; then, the values of the link fields are 1 for U(1) or $1_{2\times 2}$ for SU(2). However, to satisfy the Gaussian constraint

$$\begin{aligned}\partial_0\partial_j Y_j - g'\,\mathrm{Im}[\Phi^\dagger\partial_0\Phi] = 0,\\ \partial_0\partial_j W_j^a + g\epsilon^{abc}W_j^b\partial_0 W_j^c - g\,\mathrm{Im}[\Phi^\dagger\sigma^a\partial_0\Phi] = 0,\end{aligned} \tag{B8}$$

we must assign an initial value to the conjugate momentum field of the gauge field as follows:

$$\frac{1}{\Delta x}\sum_i \mathrm{Im}[E_i(t,x) - E_i(t,x-i)] = g'\,\mathrm{Im}[\Pi^\dagger(t,x)\Phi(t,x)], \tag{B9}$$

$$\begin{aligned}&\frac{1}{\Delta x}\mathrm{Tr}\sum_i \mathrm{i}\sigma^m[F_i(t,x) - U_i^\dagger(t,x-i)F_i(t,x-i)U_i(t,x-i)]\\ &= g\mathrm{Re}[\Pi^\dagger(t,x)\mathrm{i}\sigma^a\Phi(t,x)].\end{aligned} \tag{B10}$$

APPENDIX C: HYPERMF ON LATTICE

The MF is not well defined before the electroweak PT occurs; we therefore use a background hyperMF $\boldsymbol{B}_Y^{\rm ex} = \nabla\times\boldsymbol{Y}^{\rm ex}$ instead of MF $\boldsymbol{B}^{\rm ex} = \nabla\times\boldsymbol{A}^{\rm ex}$ [74], where $\boldsymbol{Y}^{\rm ex}$ is the space part of U(1) gauge field $Y_{\rm ex}^\mu = (Y_{\rm ex}^0, \boldsymbol{Y}_{\rm ex})$ and $\boldsymbol{A}_{\rm ex}$ is the space part of electromagnetic field $A_{\rm ex}^\mu = (A_{\rm ex}^0, \boldsymbol{A}_{\rm ex})$. In the broken phase, the relation between the two fields is $g'\boldsymbol{B}_Y^{\rm ex} = e\boldsymbol{B}^{\rm ex}$, and here $e = g\sin\theta_w$ is the electric charge.

To achieve a helical homogeneous hyperMF along the z direction, one can easily find that the U(1) field has the form

$$Y^{{\rm ex}\mu}(t,x,y,z) = (0,0,xB_Y^{\rm ex}, h_{\rm factor}LB_Y^{\rm ex}), \tag{C1}$$

since

$$\nabla\times\boldsymbol{Y}^{\rm ex} = \begin{vmatrix}\hat{x} & \hat{y} & \hat{z}\\ \partial_x & \partial_y & \partial_z\\ 0 & xB_Y^{\rm ex} & h_{\rm factor}LB_Y^{\rm ex}\end{vmatrix} = \partial_x(xB_Y^{\rm ex})\hat{z} = B_Y^{\rm ex}\hat{z}, \tag{C2}$$

where $B_Y^{\rm ex} = \frac{2}{g'}2\pi N_B L^{-2}, N_B\in\mathbb{Z}$ [93] is a constant.

For the hyperMF having the form of

$$\tilde{B}_{Yi}^{\rm ex}(\boldsymbol{k}) = B_{\rm ini}(\delta_{ij} - \hat{k}_i\hat{k}_j - \mathrm{i}\sigma_{\rm M}\varepsilon_{ijl}\hat{k}_l)g_j(\boldsymbol{k})\mathcal{P}(k), \tag{C3}$$

in Fourier space, we can first verify that

$$\tilde{Y}_l^{\rm ex}(\boldsymbol{k}) = \mathrm{i}B_{\rm ini}(\varepsilon_{lmn}\hat{k}_m - \mathrm{i}\sigma_{\rm M}\delta_{ln})g_n(\boldsymbol{k})\mathcal{P}(k)/k \tag{C4}$$

is its corresponding vector potential. Given that $\boldsymbol{B}^{\rm ex}(\boldsymbol{x}) = \nabla\times\boldsymbol{Y}^{\rm ex}(\boldsymbol{x})$, doing an inverse Fourier transform gives

$$\int\frac{\mathrm{d}^3\boldsymbol{k}}{(2\pi)^3}\tilde{\boldsymbol{B}}^{\rm ex}(\boldsymbol{k})e^{\mathrm{i}\boldsymbol{k}\cdot\boldsymbol{x}} = \nabla\times\int\frac{\mathrm{d}^3\boldsymbol{k}}{(2\pi)^3}\tilde{\boldsymbol{Y}}^{\rm ex}(\boldsymbol{k})e^{\mathrm{i}\boldsymbol{k}\cdot\boldsymbol{x}} \tag{C5}$$

$$= \int\frac{\mathrm{d}^3\boldsymbol{k}}{(2\pi)^3}\mathrm{i}\boldsymbol{k}\times\tilde{\boldsymbol{Y}}^{\rm ex}(\boldsymbol{k})e^{\mathrm{i}\boldsymbol{k}\cdot\boldsymbol{x}}. \tag{C6}$$

From this, we get $\tilde{\boldsymbol{B}}^{\rm ex}(\boldsymbol{k}) = \mathrm{i}\boldsymbol{k}\times\tilde{\boldsymbol{Y}}^{\rm ex}(\boldsymbol{k})$ or $\tilde{B}_i^{\rm ex}(\boldsymbol{k}) = \mathrm{i}\varepsilon_{ijl}k_j\tilde{Y}_l^{\rm ex}(\boldsymbol{k})$. Then, using (C4), we have

$$\begin{aligned}\mathrm{i}\varepsilon_{ijl}k_j\tilde{Y}_l^{\rm ex}(\boldsymbol{k}) &= -\varepsilon_{ijl}k_jB_{\rm ini}(\varepsilon_{lmn}\hat{k}_m - \mathrm{i}\sigma_{\rm M}\delta_{ln})g_n(\boldsymbol{k})\mathcal{P}(k)/k\\ &= -B_{\rm ini}[(\delta_{im}\delta_{jn} - \delta_{\rm in}\delta_{jm})\hat{k}_m\hat{k}_j\\ &\quad - \mathrm{i}\sigma_{\rm M}\varepsilon_{ijn}\hat{k}_j]g_n(\boldsymbol{k})\mathcal{P}(k)\\ &= B_{\rm ini}(-\hat{k}_i\hat{k}_n + \delta_{\rm in} + \mathrm{i}\sigma_{\rm M}\varepsilon_{ijn}\hat{k}_j)g_n(\boldsymbol{k})\mathcal{P}(k)\\ &= B_{\rm ini}(\delta_{ij} - \hat{k}_i\hat{k}_j - \mathrm{i}\sigma_{\rm M}\varepsilon_{ijl}\hat{k}_l)g_j(\boldsymbol{k})\mathcal{P}(k),\end{aligned} \tag{C7}$$

which is consistent with (C3).

To obtain the background hyperMF of (C3), one should follow the steps below:

(i) Step 1 is to generate a δ-correlated Gaussian distributed random vector field $\boldsymbol{g}(\boldsymbol{x})$ in coordinate space.
(ii) Step 2 is to perform Fourier transform on $\boldsymbol{g}(\boldsymbol{x})$ and get $\boldsymbol{g}(\boldsymbol{k}) = \int\mathrm{d}^3\boldsymbol{x}\boldsymbol{g}(\boldsymbol{x})e^{-\mathrm{i}\boldsymbol{k}\cdot\boldsymbol{x}}$.
(iii) Step 3 is that, according to (C4), we can get $\tilde{\boldsymbol{Y}}^{\rm ex}(\boldsymbol{k})$.
(iv) Step 4 is to perform an inverse Fourier transform on $\tilde{\boldsymbol{Y}}^{\rm ex}(\boldsymbol{k})$ to obtain $\boldsymbol{Y}^{\rm ex}(\boldsymbol{x}) = \int\mathrm{d}^3\boldsymbol{k}\tilde{\boldsymbol{Y}}^{\rm ex}(\boldsymbol{k})e^{\mathrm{i}\boldsymbol{k}\cdot\boldsymbol{x}}/(2\pi)^3$.
(v) Step 5 is that, using (A4), we can finally obtain the distribution of the link field $V_i^{\rm ex}$ on the lattice.

Next, we evaluate the ratio $kh_Y(k)/\rho_{BY}(k)$ to establish the correspondence between the helicity parameter $h_{\rm factor}$ used in the homogeneous field configuration and $\sigma_{\rm M}$ employed for fields with a spectral distribution. The relevant quantities are defined as

$$kh_Y(k) = k\tilde{Y}_i^{\rm ex}(\boldsymbol{k})\tilde{B}_{Yi}^{{\rm ex}*}(\boldsymbol{k}) = 4VB_{\rm ini}^2\sigma_{\rm M}\mathcal{P}^2(k), \tag{C8}$$

$$\rho_{BY}(k) = \tilde{B}_{Yi}^{\rm ex}(\boldsymbol{k})\tilde{B}_{Yi}^{{\rm ex}*}(\boldsymbol{k}) = 2VB_{\rm ini}^2(1+\sigma_{\rm M}^2)\mathcal{P}^2(k). \tag{C9}$$

In the limit where the spectral distribution approaches a delta function, $\mathcal{P}(k) = \delta(k)$, the background MF becomes homogeneous. While $h_Y(k)\propto\delta^2(k)/k$ appears singular in this limit, we can robustly define the physical helicity factor by integrating these spectral densities over momentum space: $h_{\rm factor} = \int\mathrm{d}^3\boldsymbol{k}\,kh_Y(k)/\int\mathrm{d}^3\boldsymbol{k}\rho_{BY}(k) = 2\sigma_{\rm M}/(1+\sigma_{\rm M}^2)$. This relation ensures a consistent mapping between the two parameters; specifically, for $\sigma_{\rm M} = 0,\pm1$, the helicity factor simplifies to $h_{\rm factor} = 0,\pm1$, respectively, maintaining the physical interpretation of the field's chirality.

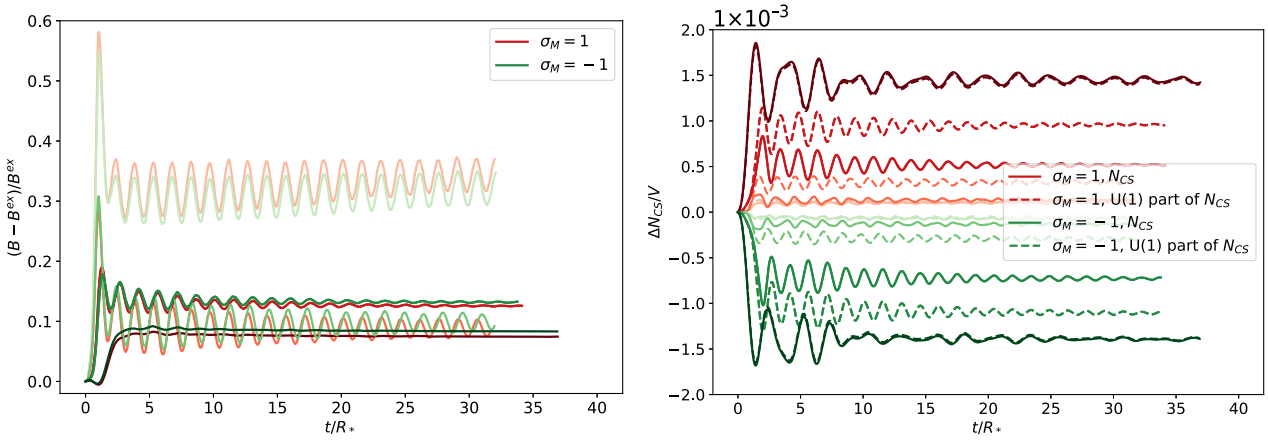


FIG. 7. Left: time evolution of the ratio between the PT-generated MF strength (with the preexisting background field subtracted) and the background field strength, $(B - B^{\rm ex})/B^{\rm ex}$, for various background field magnitudes and helicities. Right: time evolution of the Chern-Simons number density $\Delta N_{\rm CS}/V$ (solid lines) alongside its $U(1)$ component (dashed lines) under the same physical conditions. In these cases, the background field follows a spectral distribution with a finite correlation length ($N = 128, \lambda_B \sim R_*/4$). The increasing intensity of the field strength is represented by progressively darker line colors. The red lines denote the positive maximum helicity ($\sigma_{\rm M} = 1$), while the green lines correspond to the negative maximum helicity ($\sigma_{\rm M} = -1$).

APPENDIX D: EVOLUTION OF THE MF STRENGTH AND CHERN-SIMONS NUMBER DURING THE PHASE TRANSITION

Analogous to Fig. 1 in the main text, we present the time evolution of the MF strength and $\Delta N_{\rm CS}$ during the phase transition in the presence of a background MF with a finite correlation length. Figure 7 illustrates the results for a relatively short correlation length ($\lambda_B \sim R_*/4$), while Fig. 8 displays the case with a longer correlation scale ($\lambda_B \sim R_*$). Compared to the homogeneous background MF configuration, the MF generated during the PT exhibits a slightly lower magnitude; however, the $U(1)$ component of $\Delta N_{\rm CS}$ remains the dominant contribution to the total change, consistent with our primary findings.

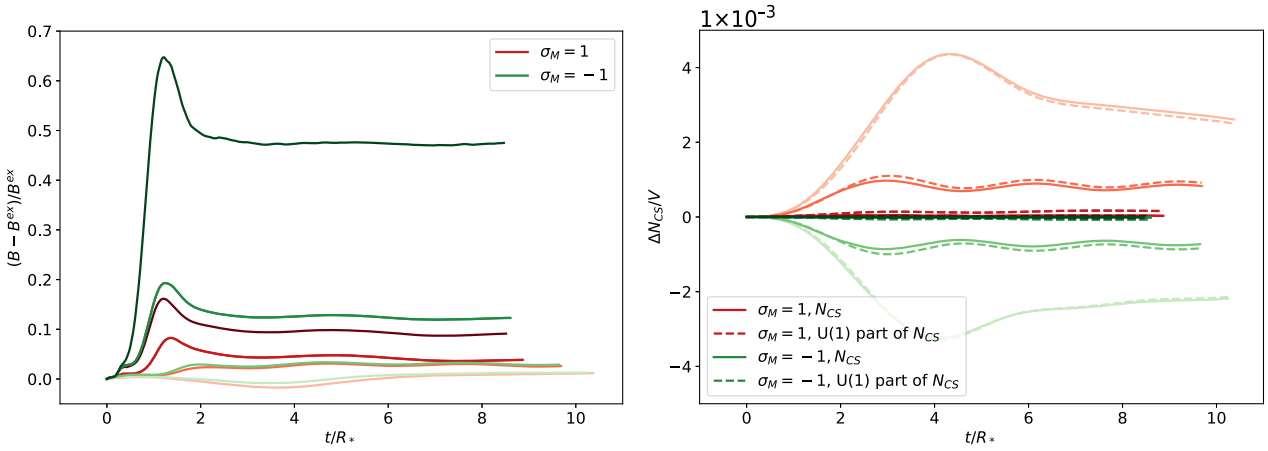


FIG. 8. Left: time evolution of the ratio between the PT-generated MF strength (with the preexisting background field subtracted) and the background field strength, $(B - B^{\rm ex})/B^{\rm ex}$, for various background field magnitudes and helicities. Right: time evolution of the Chern-Simons number density $\Delta N_{\rm CS}/V$ (solid lines) and its $U(1)$ component (dashed lines) under identical conditions. In this setup, the background field follows a spectral distribution with a longer correlation length ($N = 512, \lambda_B \sim R_*$). The increasing field strength is indicated by progressively darker line colors. The red lines denote the positive maximum helicity ($\sigma_{\rm M} = 1$), while the green lines correspond to the negative maximum helicity ($\sigma_{\rm M} = -1$).

[1] A. G. Cohen, D. B. Kaplan, and A. E. Nelson, Annu. Rev. Nucl. Part. Sci. **43**, 27 (1993).
[2] D. E. Morrissey and M. J. Ramsey-Musolf, New J. Phys. **14**, 125003 (2012).
[3] S. Davidson, E. Nardi, and Y. Nir, Phys. Rep. **466**, 105 (2008).
[4] W. Buchmuller, R. D. Peccei, and T. Yanagida, Annu. Rev. Nucl. Part. Sci. **55**, 311 (2005).
[5] W. Buchmuller, P. Di Bari, and M. Plumacher, Ann. Phys. (Amsterdam) **315**, 305 (2005).
[6] I. Affleck and M. Dine, Nucl. Phys. **B249**, 361 (1985).
[7] M. Dine, L. Randall, and S. D. Thomas, Nucl. Phys. **B458**, 291 (1996).
[8] S. L. Adler, Phys. Rev. **177**, 2426 (1969).
[9] J. S. Bell and R. Jackiw, Nuovo Cimento A **60**, 47 (1969).
[10] G. 't Hooft, Phys. Rev. Lett. **37**, 8 (1976).
[11] G. 't Hooft, Phys. Rev. D **14**, 3432 (1976); **18**, 2199(E) (1978).
[12] M. Giovannini and M. E. Shaposhnikov, Phys. Rev. Lett. **80**, 22 (1998).
[13] M. Giovannini and M. E. Shaposhnikov, Phys. Rev. D **57**, 2186 (1998).
[14] M. Joyce and M. E. Shaposhnikov, Phys. Rev. Lett. **79**, 1193 (1997).
[15] R. Wielebinski, Magnetic fields in the milky way, derived from radio continuum observations and faraday rotation studies, in *Cosmic Magnetic Fields*, edited by R. Wielebinski and R. Beck (Springer, Berlin, Heidelberg, 2005), pp. 89–112.
[16] T. E. Clarke, P. P. Kronberg, and H. Böhringer, Astrophys. J. **547**, L111 (2001).
[17] A. Bonafede, L. Feretti, M. Murgia, F. Govoni, G. Giovannini, D. Dallacasa, K. Dolag, and G. B. Taylor, Astron. Astrophys. **513**, A30 (2010).
[18] L. Feretti, G. Giovannini, F. Govoni, and M. Murgia, Astron. Astrophys. Rev. **20**, 54 (2012).
[19] K. Dolag, M. Kachelriess, S. Ostapchenko, and R. Tomàs, Astrophys. J. **727**, L4 (2010).
[20] F. Tavecchio, G. Ghisellini, L. Foschini, G. Bonnoli, G. Ghirlanda, and P. Coppi, Mon. Not. R. Astron. Soc. **406**, L70 (2010).
[21] F. Tavecchio, G. Ghisellini, G. Bonnoli, and L. Foschini, Mon. Not. R. Astron. Soc. **414**, 3566 (2011).
[22] I. Vovk, A. M. Taylor, D. Semikoz, and A. Neronov, Astrophys. J. **747**, L14 (2012).
[23] M. S. Turner and L. M. Widrow, Phys. Rev. D **37**, 2743 (1988).
[24] J. Martin and J. Yokoyama, J. Cosmol. Astropart. Phys. 01 (2008) 025.
[25] B. Ratra, Astrophys. J. Lett. **391**, L1 (1992).
[26] K. Subramanian, Astron. Nachr. **331**, 110 (2009).
[27] K. E. Kunze, Phys. Rev. D **81**, 043526 (2010).
[28] P. Adshead, J. T. Giblin, T. R. Scully, and E. I. Sfakianakis, J. Cosmol. Astropart. Phys. 10 (2016) 039.
[29] S. Kanno, J. Soda, and M.-a. Watanabe, J. Cosmol. Astropart. Phys. 12 (2009) 009.
[30] C. J. Hogan, Phys. Rev. Lett. **51**, 1488 (1983).
[31] Y. Di, J. Wang, R. Zhou, L. Bian, R.-G. Cai, and J. Liu, Phys. Rev. Lett. **126**, 251102 (2021).
[32] K. Enqvist and P. Olesen, Phys. Lett. B **319**, 178 (1993).
[33] J. Yang and L. Bian, Phys. Rev. D **106**, 023510 (2022).
[34] T. Vachaspati, Phys. Lett. B **265**, 258 (1991).
[35] G. Baym, D. Bodeker, and L. D. McLerran, Phys. Rev. D **53**, 662 (1996).
[36] D. Grasso and A. Riotto, Phys. Lett. B **418**, 258 (1998).
[37] J. M. Quashnock, A. Loeb, and D. N. Spergel, Astrophys. J. Lett. **344**, L49 (1989).
[38] D. Grasso and H. R. Rubinstein, Phys. Rep. **348**, 163 (2001).
[39] L. M. Widrow, Rev. Mod. Phys. **74**, 775 (2002).
[40] R. M. Kulsrud and E. G. Zweibel, Rep. Prog. Phys. **71**, 046901 (2008).
[41] A. Kandus, K. E. Kunze, and C. G. Tsagas, Phys. Rep. **505**, 1 (2011).
[42] L. M. Widrow, D. Ryu, D. R. G. Schleicher, K. Subramanian, C. G. Tsagas, and R. A. Treumann, Space Sci. Rev. **166**, 37 (2011).
[43] R. Durrer and A. Neronov, Astron. Astrophys. Rev. **21**, 62 (2013).
[44] A. Neronov and I. Vovk, Science **328**, 73 (2010).
[45] A. M. Taylor, I. Vovk, and A. Neronov, Astron. Astrophys. **529**, A144 (2011).
[46] C. D. Dermer, M. Cavadini, S. Razzaque, J. D. Finke, J. Chiang, and B. Lott, Astrophys. J. **733**, L21 (2011).
[47] L. Campanelli and M. Giannotti, Phys. Rev. D **72**, 123001 (2005).
[48] Y. Luo, T. Kajino, M. Kusakabe, and G. J. Mathews, Astrophys. J. **872**, 172 (2019).
[49] A. Mack, T. Kahniashvili, and A. Kosowsky, Phys. Rev. D **65**, 123004 (2002).
[50] K. Subramanian, Rep. Prog. Phys. **79**, 076901 (2016).
[51] K. Jedamzik, V. Katalinic, and A. V. Olinto, Phys. Rev. Lett. **85**, 700 (2000).
[52] S. K. Sethi and K. Subramanian, Mon. Not. R. Astron. Soc. **356**, 778 (2005).
[53] S. Saga, A. Ota, H. Tashiro, and S. Yokoyama, Mon. Not. R. Astron. Soc. **490**, 4419 (2019).
[54] T. Kahniashvili, A. Brandenburg, R. Durrer, A. G. Tevzadze, and W. Yin, J. Cosmol. Astropart. Phys. 12 (2017) 002.
[55] M. D'Onofrio, K. Rummukainen, and A. Tranberg, Phys. Rev. Lett. **113**, 141602 (2014).
[56] M. Hindmarsh, M. Lüben, J. Lumma, and M. Pauly, SciPost Phys. Lecture Notes **24**, 1 (2021).
[57] R. Caldwell *et al.*, Gen. Relativ. Gravit. **54**, 156 (2022).
[58] P. Athron, C. Balázs, A. Fowlie, L. Morris, and L. Wu, Prog. Part. Nucl. Phys. **135**, 104094 (2024).
[59] A. D. Sakharov, Pis'ma Zh. Eksp. Teor. Fiz. **5**, 32 (1967).
[60] T. Cohen, D. E. Morrissey, and A. Pierce, Phys. Rev. D **86**, 013009 (2012).
[61] S. Navas *et al.* (Particle Data Group), Phys. Rev. D **110**, 030001 (2024).
[62] A. Mazumdar and G. White, Rep. Prog. Phys. **82**, 076901 (2019).
[63] C. Caprini *et al.*, J. Cosmol. Astropart. Phys. 04 (2016) 001.
[64] C. Caprini *et al.*, J. Cosmol. Astropart. Phys. 03 (2020) 024.
[65] R. Roshan and G. White, Rev. Mod. Phys. **97**, 015001 (2025).

[66] P. Amaro-Seoane *et al.* (LISA Collaboration), arXiv:1702.00786.
[67] W.-H. Ruan, Z.-K. Guo, R.-G. Cai, and Y.-Z. Zhang, Int. J. Mod. Phys. A **35**, 2050075 (2020).
[68] J. Luo *et al.*, Classical Quantum Gravity **33**, 035010 (2016).
[69] N. K. Nielsen and P. Olesen, Nucl. Phys. **B144**, 376 (1978).
[70] S. W. MacDowell and O. Törnkvist, Phys. Rev. D **45**, 3833 (1992).
[71] A. Salam and J. Strathdee, Nucl. Phys. **B90**, 203 (1975).
[72] A. Linde, Phys. Lett. **62B**, 435 (1976).
[73] J. Ambjørn, Phys. Lett. B **220**, 659 (1989).
[74] M. Chernodub, V. Goy, and A. Molochkov, Phys. Rev. Lett. **130**, 111802 (2023).
[75] J. Annala and K. Rummukainen, Phys. Rev. D **107**, 073006 (2023).
[76] D. L. J. Ho and A. Rajantie, Phys. Rev. D **102**, 053002 (2020).
[77] D. Comelli, D. Grasso, M. Pietroni, and A. Riotto, Phys. Lett. B **458**, 304 (1999).
[78] K. Kajantie, M. Laine, J. Peisa, K. Rummukainen, and M. E. Shaposhnikov, Nucl. Phys. **B544**, 357 (1999).
[79] K. Kamada and A. J. Long, Phys. Rev. D **94**, 123509 (2016).
[80] K. Kamada and A. J. Long, Phys. Rev. D **94**, 063501 (2016).
[81] A. Abada *et al.* (FCC Collaboration), Eur. Phys. J. C **79**, 474 (2019).
[82] N. Arkani-Hamed, T. Han, M. Mangano, and L.-T. Wang, Phys. Rep. **652**, 1 (2016).
[83] V. Guada, M. Nemevšek, and M. Pintar, Comput. Phys. Commun. **256**, 107480 (2020).
[84] G. 't Hooft, Nucl. Phys. **B79**, 276 (1974).
[85] G. D. Moore, Phys. Rev. D **59**, 014503 (2002).
[86] T. Vachaspati, Rep. Prog. Phys. **84**, 074901 (2021).
[87] D. Grasso and H. R. Rubinstein, Phys. Rep. **348**, 163 (2001).
[88] A. Rajantie, P. M. Saffin, and E. J. Copeland, Phys. Rev. D **63**, 123512 (2001).
[89] Y. Zhang, F. Ferrer, and T. Vachaspati, Phys. Rev. D **96**, 043014 (2017).
[90] Y. Zhang, T. Vachaspati, and F. Ferrer, Phys. Rev. D **100**, 083006 (2019).
[91] D. Daverio, M. Hindmarsh, and N. Bevis, arXiv:1508.05610.
[92] G. Guennebaud, B. Jacob *et al.*, Eigen, https://libeigen.gitlab.io (2010).
[93] G. S. Bali, F. Bruckmann, G. Endrődi, Z. Fodor, S. D. Katz, S. Krieg, A. Schäfer, and K. K. Szabó, J. High Energy Phys. 02 (2012) 044.
[94] Y. Di, L. Bian, and R.-G. Cai, Phys. Rev. D **113**, 043529 (2026).
[95] A. Brandenburg, R. Durrer, Y. Huang, T. Kahniashvili, S. Mandal, and S. Mukohyama, Phys. Rev. D **102**, 023536 (2020).
[96] A. Brandenburg, R. Durrer, Y. Huang, T. Kahniashvili, S. Mandal, and S. Mukohyama, Phys. Rev. D **102**, 023536 (2020).
[97] T. Kahniashvili, A. Brandenburg, and A. G. Tevzadze, Phys. Scr. **91**, 104008 (2016).
[98] A. Brandenburg, Y. He, and R. Sharma, Astrophys. J. **922**, 192 (2021).
[99] H. Abdalla *et al.* (CTA Collaboration), J. Cosmol. Astropart. Phys. 02 (2021) 048.
[100] A. Abramowski *et al.* (H. E. S. S. Collaboration), Astron. Astrophys. **562**, A145 (2014).
[101] J. Aleksic *et al.* (MAGIC Collaboration), Astron. Astrophys. **524**, A77 (2010).
[102] S. Archambault *et al.* (VERITAS Collaboration), Astrophys. J. **835**, 288 (2017).
[103] M. Ackermann *et al.* (Fermi-LAT Collaboration), Astrophys. J. Suppl. Ser. **237**, 32 (2018).
[104] T. Fujita and K. Kamada, Phys. Rev. D **93**, 083520 (2016).
[105] C. J. Copi, F. Ferrer, T. Vachaspati, and A. Achúcarro, Phys. Rev. Lett. **101**, 171302 (2008).
[106] T. Vachaspati, Phys. Rev. Lett. **87**, 251302 (2001).
[107] T. Vachaspati and G. B. Field, Phys. Rev. Lett. **73**, 373 (1994).
[108] M. Barriola, Phys. Rev. D **51**, R300 (1995).
[109] A. Achucarro and T. Vachaspati, Phys. Rep. **327**, 347 (2000).
[110] M. Goodband and M. Hindmarsh, Phys. Lett. B **363**, 58 (1995).
[111] M. James, L. Perivolaropoulos, and T. Vachaspati, Nucl. Phys. **B395**, 534 (1993).
[112] L. Bian, S. Ge, J. Shu, B. Wang, X.-Y. Yang, and J. Zong, Phys. Rev. D **109**, L101301 (2024).
[113] A. Afzal *et al.* (NANOGrav Collaboration), Astrophys. J. Lett. **951**, L11 (2023); **971**, L27(E) (2024).